Periodic Nanoslot Patterns as an Effective Approach to Improving the Thermoelectric Performance of Thin Films

Qing Hao* and Yue Xiao

Department of Aerospace and Mechanical Engineering, University of Arizona, Tucson, Arizona 85721-0119, USA

(Received 23 January 2020; revised manuscript received 24 March 2020; accepted 7 May 2020; published 8 June 2020)

For thermoelectric applications, thermoelectric Si thin films with periodic circular pores have been intensively studied because of the low price and earth abundance of Si. In this work, a different periodic nanoporous pattern is investigated for its potential thermoelectric benefit, i.e., a Si thin film with periodic nanoslots. Inside such structures, the neck between adjacent nanoslots functions as the nanorestriction to suppress the phonon transport, leading to a dramatically reduced lattice thermal conductivity. When the neck width is still longer than the mean free paths of majority charge carriers, bulklike electron transport can be maintained so that the thermoelectric ZT can be enhanced. For the thermal designs of these porous thin films, a simple but accurate analytical model based on the mean-free-path modification with a characteristic length is derived and is used to predict their thermoelectric properties. For heavily doped Si films with the neck width reduced to 5 nm, the computed ZT can reach 0.58 at 1100 K. The proposed nanoslot pattern can be extended to general thin films and atomic thick materials to tune their transport properties.

DOI: 10.1103/PhysRevApplied.13.064020

I. INTRODUCTION

Thermal transport within nanostructured materials is one central topic for nanotechnology, with wide applications in thermal insulation, thermal management of electronics, and solid-state thermoelectric (TE) energy conversion [1,2]. Particularly for TE applications, a good TE material should possess a high electrical conductivity σ, a high Seebeck coefficient S, and a low thermal conductivity k. The combination of these is required to achieve a high dimensionless ZT, defined as $ZT = (S^2\sigma T)/k = (S^2\sigma T)/(k_L + k_E)$. Here T is the absolute temperature, k_L is the lattice part of k, and k_E is the electronic part of k [3]. In nanostructured materials, k_L can often be dramatically reduced with phonon scattering by nanostructured interfaces or boundaries [4–6], with concurrently maintained or sometimes improved electrical properties [7,8]. A high ZT can thus be achieved with such decoupling of electrical and thermal properties.

Besides various nanostructured bulk materials [4,8,9], attention has also been paid to periodic nanoporous thin films [2,10–18] or two-dimensional (2D) materials with atomic thickness [19–21], which can be used for device-cooling applications. Such a periodic nanoporous pattern can be exactly defined in nanofabrication. A room-temperature $ZT \approx 0.4$ was reported for hexagonal periodic nanoporous Si film with neck and pitch sizes of 23 and 55 nm, respectively [10]. In a more recent study with more accurate TE measurements, $ZT \approx 0.05$ at room temperature was instead found for similar samples with a neck width of 24 nm between adjacent nanopores and at a doping level of 2.0×10^{19} cm^{-3} [12]. This lower ZT was attributed to the use of ion implantation for doping, which led to a largely reduced electrical conductivity.

Despite numerous studies on periodic nanoporous Si films with pores distributed across a square or hexagonal lattice, the associated analytical modeling has been a challenge, which largely hinders the thermal designs of these nanoporous materials. At the ballistic limit, the characteristic length $L_c = (4p^2 - \pi d^2)/\pi d$ has been used to modify the phonon mean free paths (MFPs) for k_L predictions [22,23]. In physics, this L_c is the geometric mean beam length (MBL) for films with aligned nanopores that have a pitch p and pore diameter d. However, k_L predictions using this L_c become less accurate with increased diffuse phonon transport, mainly due to the error of using Matthiessen's rule to combine internal and boundary phonon scattering [22,24,25]. Other characteristic lengths include $L_c = \sqrt{p^2 - \pi d^2/4}$ as the square root of the solid area within a period [26], $L_c = p - d$ as the neck width [27,28], and $L_c \sim 4p^2/\pi d$ as the reciprocal of the surface-to-volume ratio [29]. Errors can be found between an analytical model using these L_c values and accurate predictions by solving the phonon Boltzmann transport equation [22,24].

In this work, a different nanoporous pattern is evaluated for its ZT potential, i.e., periodic nanoslots patterned across a thin film. Figure 1 illustrates a thin film patterned with aligned nanoslots. For phonons with MFPs much longer than the neck width w between adjacent nanoslots, these phonons will travel ballistically away from the neck,

*qinghao@email.arizona.edu

leading to strongly suppressed thermal transport and an associated ballistic thermal resistance [30,31]. On the other hand, charge carriers with usually a much shorter MFP are less affected by nanoslot patterns and thus bulklike electrical properties can be preserved. The overall ZT can be enhanced. Compared with nanowires with classical phonon size effects for similar ZT enhancement [32], nanoslot-patterned thin films can carry a much larger heat flow and can be easily integrated with electronic devices for cooling applications. Different from films with circular nanopores, an accurate L_c expression is developed for fast ZT evaluations in this work. The proposed modeling can be widely used for the materials design of such nanoslot-patterned thin films and similar nanoslot-patterned atomic layer materials [31].

As an advancement, the proposed L_c expression found in this work that provides a fast way to predict the TE properties of nanoslot-patterned thin films with arbitrary thickness. No other analytical model has been proposed previously for these nanoslot-patterned thin films. In this aspect, previous studies employ complicated techniques such as Monte Carlo (MC) simulations [33,34] or numerically solving the phonon or electron Boltzmann transport equation (BTE) [35]. These methods can be very time consuming and technically demanding, particularly when frequency-dependent phonon MFPs are considered. In contrast, the proposed analytical model is simply based on the phonon MFP modification and can be easily adopted in the materials design of these porous films, where a quick evaluation of the material properties is required.

II. ANALYTICAL MODELING TO PREDICT TE PROPERTIES

To predict the in-plane TE properties of nanoslot-patterned thin films, an analytical model is derived for a nanoslot-patterned thin film with the periodic length (pitch) l along the heat-flow direction, neck width w between adjacent nanoslots, neck depth b, film thickness t, and the nanoslot pitch p along the transverse direction (Fig. 1 inset). The analytical model is developed for phonon transport but the same size effects are anticipated for charge carriers as well. For a small neck depth b, the thermal and electrical resistances of the rectangular-nanowire neck region can be neglected in the modeling. The analytical model is further extended in Sec. III B for the treatment of a large neck depth b.

A. Characteristic length of a 2D thin film with patterned periodic nanoslots

For phonons traveling out of the neck region between adjacent nanoslots, a ballistic thermal resistance is developed and becomes larger with decreased neck width w. For the whole periodic structure, a characteristic length L_c is derived assuming ballistic phonon transport and a very small b value, i.e., no additional thermal resistance along the neck region as a rectangular nanowire. This L_c is anticipated to be accurate across the whole phonon MFP spectrum. A similar result can be found for a thin film with a single row of periodic nanoslots patterned in its middle [30].

Along the heat-flow direction (i.e., the x direction in Fig. 2), a periodic heat-flux boundary condition is applied to a nanoslot-patterned thin film [33]. Due to the structure symmetry, phonons are enforced to be specularly reflected on the sidewalls of one period. This boundary condition dictates that the distortion of the distribution function from the equilibrium distribution is periodic on the hot and cold ends of one period [Fig. 1(b)]. In calculations, a uniform virtual-wall temperature is assigned to both ends, i.e., T_1 for the hot end and T_2 for the cold end. The boundary condition can be written as

$$f_2^-(\theta,\psi,\omega,y,z) - f_0(T_2,\omega) = f_1^-(\theta,\psi,\omega,y,z) - f_0(T_1,\omega), \tag{1a}$$

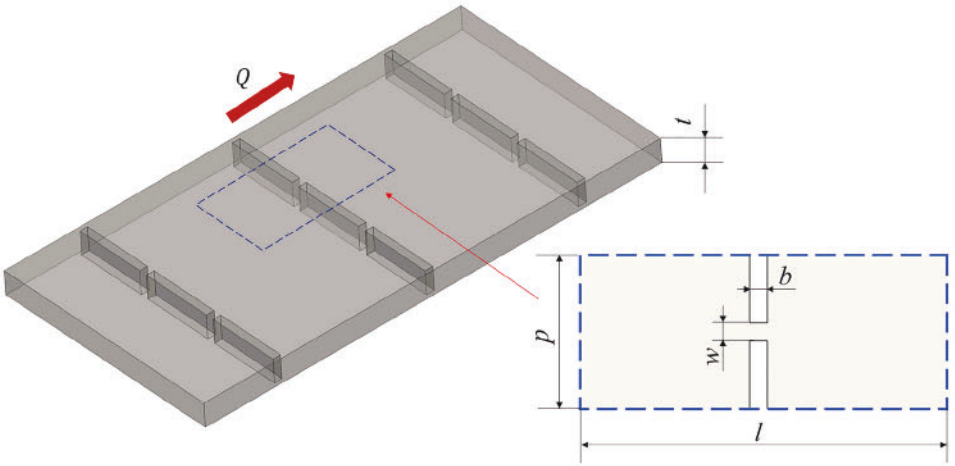

FIG. 1. Thin film with periodic nanoslots. The inset shows dimensions for one single period.

$$f_2^+(\theta,\psi,\omega,y,z) - f_0(T_2,\omega) = f_1^+(\theta,\psi,\omega,y,z) - f_0(T_1,\omega), \tag{1b}$$

in which f is the distribution function, θ is the polar angle, ψ is the azimuthal angle, ω is the phonon angular frequency, T is the absolute temperature, y and z are locations within the y-z plane for each end. The subscripts "1" and "2" denote the hot wall ($x = 0$) and cold wall ($x = l$), respectively. The superscripts "+" and "−" represent the positive x and negative x directions, respectively. Given as the Bose-Einstein distribution for phonons, $f_0(T_1,\omega)$ and $f_0(T_2,\omega)$ are the equilibrium distribution function at the corresponding local virtual-wall temperatures. The general $f_0(T,\omega)$ is isotropic and is given as

$$f_0(T,\omega) = \frac{1}{\exp\left(\frac{\hbar\omega}{k_B T}\right) - 1}, \tag{2}$$

where $\hbar$ is the reduced Planck constant and k_B is the Boltzmann constant.

When phonons have completely ballistic transport, phonons moving into the neck region are emitted from the hot wall at $x = 0$ and the cold wall at $x = l$. These phonons are associated with the distribution functions $f_1^+(\theta,\psi,\omega,y,z)$ and $f_2^-(\theta,\psi,\omega,y,z)$. The incoming heat flow Q_1 (Fig. 2) due to phonons emitted from the hot wall is given as

$$\frac{Q_1}{wt} = \langle f_1^+ \rangle, \tag{3}$$

with the general integration $\langle f \rangle$ defined as

$$\langle f \rangle = \frac{1}{4\pi} \sum\nolimits_{i=3} \int_{\psi=0}^{2\pi} \int_{\omega=0}^{\omega_{\max,i}} \times \int_{\theta} [\hbar\omega v_{g,i}(\omega) D_i(\omega) \cos\theta \sin\theta] f \, d\omega \, d\psi \, d\theta. \tag{4}$$

For $\langle f_1^+ \rangle$ in Eq. (3), θ integration is from 0 to $\frac{\pi}{2}$, whereas θ integration is from $\frac{\pi}{2}$ to π for the integration of a negative-x-direction distribution function, e.g., $\langle f_2^- \rangle$. In Eq. (4), $\omega_{\max,i}$, $v_{g,i}(\omega)$, and $D_i(\omega)$ are the maximum phonon angular frequency, phonon group velocity, and phonon density of states (DOS), respectively. The subscript i represents three acoustic phonon branches, whereas the optical branches are neglected for their contribution to the heat conduction. For any incident location $\vec{R}$ within an imaginary y-z plane for the left side of the neck region at $x = (l - b)/2$, the corresponding hot-wall emission location within the y-z plane for the hot wall at $x = 0$ can be back tracked with the incident angles that depends on θ and ψ for the corresponding hot-wall emission. Ballistic phonon transport is assumed here.

The part of the incoming heat flow associated with $f_0(T_1)$ for the hot-wall emission is

$$\frac{Q_{T_1}}{wt} = \langle f_0(T_1) \rangle . \tag{5}$$

Subtracting Eq. (5) from Eq. (4) yields

$$\frac{Q_1}{wt} - \frac{Q_{T_1}}{wt} = \langle f_1^+ \rangle - \langle f_0(T_1) \rangle . \tag{6}$$

A similar equation can be found for heat flow Q_2 emitted from the cold wall to the neck region:

$$\frac{Q_2}{wt} - \frac{Q_{T_2}}{wt} = \langle f_2^- \rangle - \langle f_0(T_2) \rangle . \tag{7}$$

Subtracting Eq. (7) from Eq. (6) yields the averaged net heat flux across the neck width, given as

$$\frac{Q}{wt} = \left[\langle f_1^+ \rangle - \langle f_0(T_1) \rangle\right] - \left[\langle f_2^- \rangle - \langle f_0(T_2) \rangle\right] + \frac{Q_{T_1} - Q_{T_2}}{wt}, \tag{8}$$

with $Q = Q_1 - Q_2$ as the net heat flow across the neck region with 100% transmissivity for incident phonons. This assumption is valid for ultrashort b values. Detailed discussions for this aspect can be found for thin films with rectangular pores [34] and more complicated nanostructures [36]. The extension of this model to nanoslot patterns with a large b is given in Sec. III B.

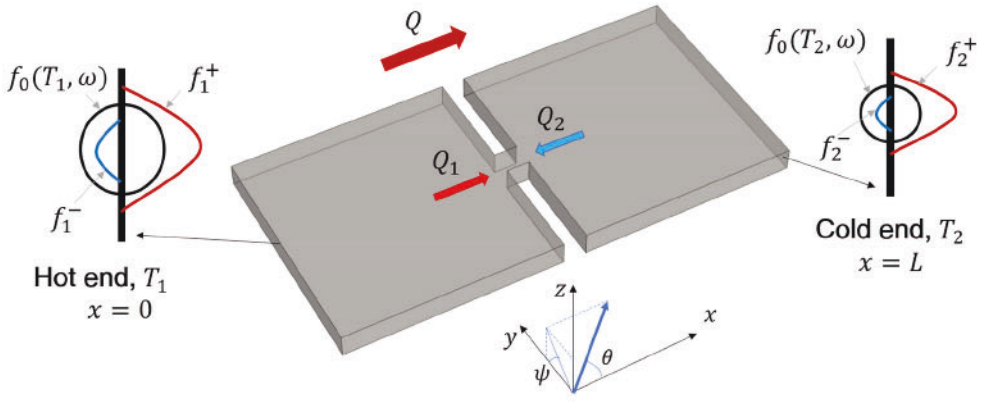

FIG. 2. Periodic boundary condition of a single period for phonon transport.

Substituting Eq. (1a) into Eq. (8) leads to

$$\frac{Q}{wt} = \langle f_1^+ \rangle - \langle f_1^- \rangle + \frac{Q_{T_1} - Q_{T_2}}{wt}, \tag{9}$$

where $\langle f_1^+ \rangle - \langle f_1^- \rangle$ on the right-hand side is approximately the net heat flux $\overline{q_{x=0}}$ averaged across the hot wall. The net heat flow Q across the neck is equal to the net heat flow across the hot wall in steady states, i.e., $Q = \overline{q_{x=0}} pt$. Equation (9) thus becomes

$$\frac{Q}{wt} \approx \frac{Q}{pt} + \frac{Q_{T_1} - Q_{T_2}}{wt},$$

or

$$Q \approx \frac{p(Q_{T_1} - Q_{T_2})}{p - w}. \tag{10}$$

The in-plane thermal conductance G of the whole structure is thus

$$\begin{aligned} G &= \lim_{\Delta T \to 0} \frac{Q}{\Delta T} \approx \frac{p}{p-w} \lim_{\Delta T \to 0} \frac{Q_{T_1} - Q_{T_2}}{\Delta T} \\ &= \frac{p}{p-w} wt \frac{\partial \langle f_0(T) \rangle}{\partial T} \\ &= \frac{p}{p-w} \frac{wt}{4} \sum\nolimits_{i=3} \int_{\omega=0}^{\omega_{\max,i}} v_{g,i}(\omega) C_i(\omega) d\omega, \end{aligned} \tag{11}$$

where $\Delta T = T_1 - T_2$ and $C_i(\omega)$ is the spectral phonon-specific heat per unit volume for phonon branch i.

A characteristic length L_c is assumed for the 2D nanoslot patterns and is used to modify the phonon MFPs from the ballistic to the diffusive regimes. Based on Matthiessen's rule, the effective phonon MFP in the nanoslot-patterned thin film is

$$1/\Lambda_{\text{eff}} = 1/\Lambda_{\text{film}} + 1/L_c, \tag{12}$$

where Λ_{film} is the effective in-plane phonon MFP within a solid film and accounts for the partially and completely diffusive phonon scattering on the top and bottom film surfaces. In this treatment, the influence of rough film top and bottom surfaces is fully incorporated into Λ_{film}. A three-dimensional (3D) thin film can be viewed as a 2D thin film with the phonon MFP Λ_{film} reduced from the bulk phonon MFP Λ_{bulk}. When Λ_{film} approaches infinity at the ballistic limit, $\Lambda_{\text{eff}} = L_c$ is obtained so that

$$G = k\frac{pt}{l} H_w = \left[\sum\nolimits_{i=3} \int_{\omega=0}^{\omega_{\max,i}} v_{g,i}(\omega) C_i(\omega) L_c d\omega / 3 \right] \frac{pt}{l} H_w, \tag{13}$$

in which the factor H_w accounts for the reduced G due to decreased cross section for heat conduction inside a porous structure. This factor H_w can be determined by Fourier's law analysis to check the in-plane thermal conductance G reduced from that for a solid thin film. In this case, H_w incorporates the porosity influence, whereas the classical phonon size effects are further included with L_c to modify the initial Λ_{film} of a solid film. The same treatment has been widely used for nanoporous thin films with periodic cylindrical nanopores through the film [22,24,37,38]. Analytical expressions of the H_w factors are available for a bulk material with cubically aligned spherical pores (Eucken factor [39,40]) and 2D patterns with periodic circular pores (Hashin-Shtrikman factor [41]). In this study, H_w of the nanoslot-patterned films is evaluated using the COMSOL Multiphysics software package.

Comparing Eq. (11) and Eq. (13) to match the spectral contribution of G by individual phonon modes, L_c should satisfy

$$L_c \approx \frac{w}{p-w} \frac{3l}{4H_w}. \tag{14a}$$

Although this L_c is derived under the ballistic limit, it is anticipated to be reasonably accurate when the phonon transport becomes more diffusive. In comparison, thin films with a single row of nanoslots sandwiched between two blackbodies yields a characteristic length as [30]

$$L_c = \frac{w}{p} \frac{3l}{4H_w}. \tag{14b}$$

The difference between Eqs. (14a) and (14b) is caused by the different boundary conditions. For a small $w \ll p$, the two L_c expressions have negligible divergence. With such simple L_c expressions, the lattice thermal conductivity k_L can be easily predicted using Eq. (12) without numerically solving the complicated phonon BTE or performing phonon MC simulations.

B. Incorporating the diffusive phonon scattering at top and bottom film surfaces

The discussion in Sec. II A is for a 2D thin film, i.e., a film with smooth top and bottom surfaces to specularly reflect phonons. In practice, the partially or completely diffusive phonon scattering by the thin-film surfaces can add resistance to phonon transport and further reduce the lattice thermal conductivity. This effect can be incorporated into the employed Λ_{film} that is modified from the bulk phonon MFP (Λ_{bulk}) by the Fuchs-Sondheimer model [42]:

$$\begin{aligned} \frac{\Lambda_{\text{film}}}{\Lambda_{\text{bulk}}} = 1 - \frac{3[1 - P(\lambda)]\Lambda_{\text{bulk}}}{2t} \int_0^1 (x - x^3) \\ \times \frac{1 - \exp\left(-\frac{t}{\Lambda_{\text{bulk}} x}\right)}{1 - P(\lambda)\exp\left(-\frac{t}{\Lambda_{\text{bulk}} x}\right)} dx, \end{aligned} \tag{15}$$

where t is the film thickness and $P(\lambda)$ is the probability of specular phonon reflection on the film surface. Based on Ziman's theory, $P(\lambda)$ depends on the phonon wavelength λ and surface roughness η, given as $P(\lambda) = \exp[-16\pi^2(\eta_1/\lambda)^2]$ [43,44]. Above 300 K, completely diffusive phonon reflection can be assumed because the typical approximately 1-nm film-surface roughness is comparable to phonon wavelengths to largely eliminate the possibility of specular reflection of phonons.

With Eq. (14a), L_c can be directly used to modify Λ_{film} and obtain an effective phonon MFP Λ_{eff} in Eq. (12), which becomes an input of the analytical solutions to predict TE properties. For classical phonon size effects, only the phonon MFPs are modified by Eq. (12) and other parameters remain the same as the bulk material. Based on the kinetic relationship, the lattice thermal conductivity k_L is given as

$$k_L = \frac{1}{3} H_w \sum_{i=1}^{3} \int_0^{\omega_{\max,i}} c_i(\omega) v_{g,i}(\omega) \Lambda_{\text{eff},i}(\omega) d\omega. \quad (16)$$

A similar treatment using Λ_{film} to incorporate the phonon size effects related to the film thickness can also be found for rectangular nanowires fabricated from thin films and other nanoporous thin films [30,38,45].

C. Extension to electrical property predictions

The treatment for phonons can be extended to charge-carrier transport by modifying the MFPs of charge carriers. For Si, a six-fold degenerate conduction band and a valence band are considered, i.e., two bands in total. For the ith valley of charge carriers, the in-plane electrical conductivity σ and the Seebeck coefficient S are expressed as [46,47]

$$\sigma_i = H_w \frac{e^2 (2 m_d^* k_B T)^{3/2}}{3 m_\chi^* \pi^2 \hbar^3} \int_0^\infty \left(-\frac{\partial f}{\partial z}\right) \tau(z) \frac{(z+\beta z^2)^{3/2}}{1+2\beta z} dz, \quad (17)$$

and

$$S_i = \frac{k_B}{e} \frac{\int_0^\infty \left(-\frac{\partial f}{\partial z}\right) \tau(z)(z-\eta) \frac{(z+\beta z^2)^{3/2}}{1+2\beta z} dz}{\int_0^\infty \left(-\frac{\partial f}{\partial z}\right) \tau(z) \frac{(z+\beta z^2)^{3/2}}{1+2\beta z} dz}. \quad (18)$$

Here the subscript i represents valley index, e is the charge per carrier, τ is the energy-dependent relaxation time of charge carriers, k_B is the Boltzmann constant, T is the absolute temperature, $\beta = k_B T/E_g$ with E_g as the band gap, and $\hbar$ is the Plank constant divided by 2π. The correction factor H_w is added to account for the influence of the nanoslot pattern. The DOS effective mass and electric susceptibility effective mass for each band are denoted by m_d^* and m_χ^*, respectively. The letter z represents the reduced charge-carrier energy $z = E/k_B T$, where E should refer to the corresponding band extrema. In addition, $f = [1 + \exp(z-\eta)]^{-1}$ is the Fermi-Dirac distribution function, in which $\eta = E_F/k_B T$ is the reduced Fermi level. With σ_i and S_i for each band, the total in-plane σ and S can be computed as

$$\sigma = \sum_i \sigma_i, \quad (19)$$

and

$$S = \frac{\sum_i \sigma_i S_i}{\sum_i \sigma_i}. \quad (20)$$

As a measure of the averaged electron energy above the Fermi level under the open-circuit condition [42], the Seebeck coefficient here is not directly affected by H_w. The impact of the nanoporosity on S can be found in the modified energy-dependent relaxation time τ of charge carriers. Some discussions can be found in a separated study [48].

The in-plane electronic thermal conductivity k_E can be expressed as

$$k_E = \sum_i k_{E,i} + \sum_{i \neq k} \frac{\sigma_i \sigma_k}{\sigma_i + \sigma_k} (S_i - S_k)^2 T, \quad (21)$$

where i and k are band indices, and k_E of band i is calculated by the Wiedemann-Franz law, i.e., $k_{E,i} = H_w L_0 \sigma_i T$. Again, H_w is added for nanoslot patterns. Here the Lorenz number L_0 is expressed as

$$L_0 = \left(\frac{k_B}{e}\right)^2 \left\{ \frac{\int_0^\infty \left(-\frac{\partial f}{\partial z}\right) \tau(z) z^2 \frac{(z+\beta z^2)^{3/2}}{1+2\beta z} dz}{\int_0^\infty \left(-\frac{\partial f}{\partial z}\right) \tau(z) \frac{(z+\beta z^2)^{3/2}}{1+2\beta z} dz} - \left[\frac{\int_0^\infty \left(-\frac{\partial f}{\partial z}\right) \tau(z) z \frac{(z+\beta z^2)^{3/2}}{1+2\beta z} dz}{\int_0^\infty \left(-\frac{\partial f}{\partial z}\right) \tau(z) \frac{(z+\beta z^2)^{3/2}}{1+2\beta z} dz} \right]^2 \right\}. \quad (22)$$

The bulk relaxation time τ_{bulk} is determined using Matthiessen's rule:

$$\tau_{\text{bulk}} = \left(\frac{1}{\tau_{\text{ac}}} + \frac{1}{\tau_{\text{im}}}\right)^{-1}, \quad (23)$$

where $1/\tau_{\text{ac}}$ and $1/\tau_{\text{im}}$ are the scattering rates for the scattering with the acoustic phonons and ionized impurities, respectively. The expressions and parameters used for τ_{ac} and τ_{im} are given elsewhere [49,50]. With τ_{bulk}, the bulk electron MFP λ_{bulk} can be expressed as $\lambda_{\text{bulk}} = \tau_{\text{bulk}} v$, where v is the group velocity of a charge carrier. With λ_{bulk} and film thickness t, Eq. (15) can be used to calculate

the electron MFP λ_{film} in a solid thin film. The effective relaxation time τ of a nanoslot-patterned thin film is

$$\tau = \left(\frac{1}{\lambda_{\text{film}}} + \frac{1}{L_c}\right)^{-1} / v. \tag{24}$$

It should be noted that the surface states and their trapped charge carriers on the nanoslot edges are not considered for their impact on electrical properties. Detailed discussions of pore-edge-trapped charges can be found for nanoporous Si films [49] and graphene antidot lattices [19]. In practice, atomic layer deposition of Al_2O_3 can be used for surface passivation to preserve bulklike electrical properties for nanoporous Si films [10].

To verify the model predictions, electron MC simulations [50] are carried out for a representative 2D thin film with a n-type doping level of 1×10^{20} cm^{-3}, $l = 100$ nm, $p = 150$ nm, $w = 50$ nm, and $b = 2$ nm. For σ, the difference between the predictions by the analytical model and the energy-dependent electron MC simulations are within 8%, which is comparable to the 5% uncertainty in typical electron MC simulations [50].

III. RESULTS AND DISCUSSIONS

A. Model verification

The proposed analytical model based on the characteristic length L_c in Eq. (14a) is validated by comparing the model predictions with those given by frequency-dependent phonon MC simulations. By tracking the movement and scattering of individual phonons, the phonon MC simulations can statistically obtain the solution of the phonon Boltzmann transport equation. All simulations employ a boundary condition based on a periodic heat flux with a constant virtual-wall temperature [33]. With this boundary condition, a single period can be used as the computational domain. With an applied virtual-wall temperature difference ΔT across the period, the lattice thermal conductivity can be computed using ΔT and the simulated heat flow across the domain. To improve the computational efficiency, a variance-reduced phonon MC technique developed by Péraud and Hadjiconstantinou is adopted [51].

Figure 3(a) compares k_L predicted with the analytical model and those predicted by frequency-dependent phonon MC simulations. The computed structure has $l = 100$–200 nm, $w = 10$–50 nm, $b = 1$ nm, $t = 100$ nm, and $p = 150$ nm. The top and bottom surfaces of the thin film are assumed to diffusively scatter phonons. Considering three acoustic branches only, the required frequency-dependent bulk phonon MFP Λ_{bulk} in Eq. (15) is from existing first-principles calculations on bulk Si [52]. The corresponding bulk phonon MFP distribution has also been verified with experiments [53]. In all simulated cases, the divergence between the analytical model and the phonon MC simulations is <5%. Figures 3(b) and 3(c) present two typical temperature profiles generated by phonon MC simulations, where the temperature gradient peaks at the neck region.

Although L_c is derived at the ballistic limit, above phonon MFP modification using L_c is anticipated to be valid across the entire phonon MFP spectrum. This assumption can be verified by examining the suppression function $\alpha(\eta) = k_L^*/k_{\text{film}}^*$ for nanoslot patterns with varied $\eta = \Lambda_{\text{film}}^*/w$. Here Λ_{film}^* is a constant in-plane phonon MFP, k_{film}^* is the in-plane lattice thermal conductivity corresponding to Λ_{film}^*, and k_L^* is the lattice thermal conductivity acquired using the modified phonon MFP, i.e., $(\Lambda_{\text{film}}^{*\,-1} + L_c^{-1})^{-1}$. This suppression function indicates the reduction of the lattice thermal conductivity from the solid-film k_{film}^* to k_L^* due to the nanoslot pattern. The constant Λ_{film}^* can vary across the whole phonon MFP spectrum to obtain the complete $\alpha(\eta)$ curves. Detailed discussions of such MFP-dependent phonon transport analysis can be found elsewhere [30,54,55]. Without losing the generality, the selected nanoslot dimensions are $p = 150$ nm, $l = 100$ nm, $b = 1$ nm, and $w = 10$–70 nm. As a result, the suppression function using L_c from Eq. (14a) is shown in

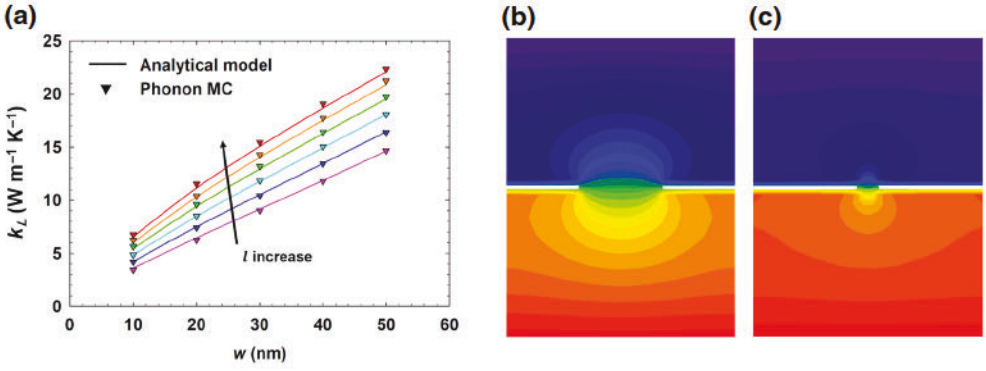

FIG. 3. (a) Lattice thermal conductivity k_L comparison between the analytical model (curves) and phonon MC simulations (triangles), with $l = 100$, 120, 140, 160, 180, and 200 nm from bottom to top curves. Temperature profiles (in Kelvin) for films with (b) $l = 200$ nm, $w = 50$ nm, and (c) $l = 200$ nm, $w = 10$ nm. Other dimensions are the same, i.e., $p = 150$ nm, $t = 100$ nm.

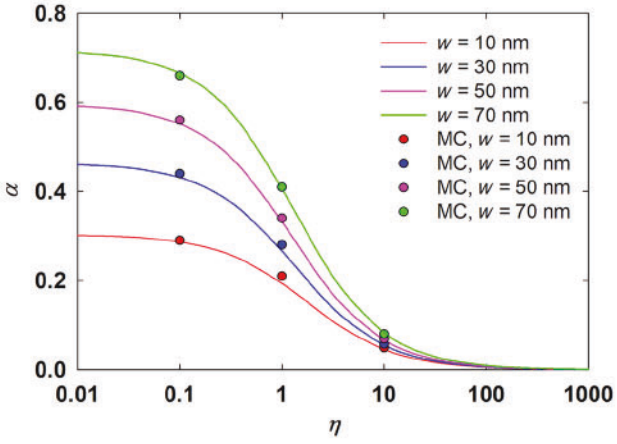

FIG. 4. Suppression function α for nanoslot-patterned films. Symbols are from frequency-independent phonon MC simulations assuming a constant in-plane phonon MFP Λ^*_{film}.

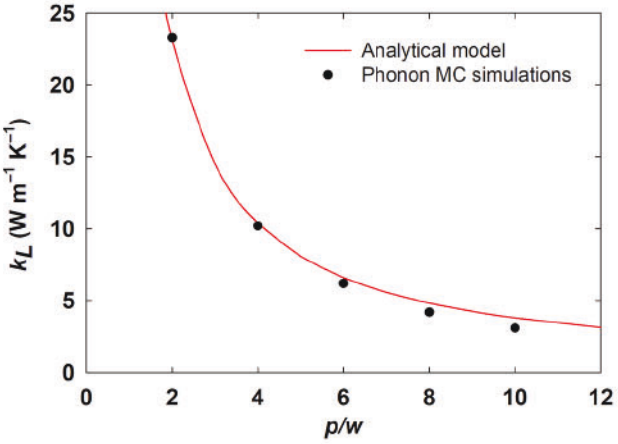

FIG. 5. Comparison between the analytical model and frequency-dependent phonon MC simulations for varied p/w ratios. Other dimensions are $l = 100$ nm, $w = 50$ nm, $b = 1$ nm, and $t = 100$ nm.

Fig. 4 as the solid lines, whereas the predictions using the frequency-independent phonon MC simulations are shown as symbols. The suppression function α has the form

$$\alpha = \frac{k_L^*}{k_{\text{film}}^*} = \frac{\left(\Lambda_{\text{film}}^{*\,-1} + L_c^{-1}\right)^{-1}}{\Lambda_{\text{film}}^*} H_w = \frac{L_c}{\eta w + L_c} H_w, \quad (25)$$

which suggests α should approach H_w at $\eta \to 0$. This trend can be observed in Fig. 4 as the curves saturate at small η values. In general, phonon MC simulations agree well with the analytical model, indicating that L_c can be used for the entire phonon MFP spectrum.

B. Model accuracy for largely varied nanoslot patterns

The analytical model based on Eq. (14a) can accommodate a wide range of geometric designs of the nanoslot, but it may become less accurate under certain conditions. In the derivation of Eq. (14a), $\langle f_1^+ \rangle - \langle f_1^- \rangle$ in Eq. (9) is approximately equal to the net heat flux $\overline{q_{x=0}}$ averaged across the virtual hot wall. However, this assumption becomes less accurate at a large p/w ratio. If a spot on the virtual hot wall is far away from the neck region shown in Fig. 1, the view factor between this spot and the neck region will be small, resulting in its weak contribution to Q_1 and thus the net heat flow Q. Such regions are "thermally dead" in the phonon transport analysis [56]. With the same weight in the evaluation of $\overline{q_{x=0}}$, a hot-wall spot with the same area can contribute significantly more to Q if this spot is directly facing the neck. This contrast between the weights in their Q contributions leads to errors in the above-mentioned assumption and such errors can further increase at larger p/l ratios. To show the influence of thermally dead regions, Fig. 5 compares the analytical model with the phonon MC simulation with increased p values. Other dimensions used are $l = 100$ nm, $w = 50$ nm, $b = 1$ nm, and $t = 100$ nm. At $p/w \geq 8$, the analytical model starts to deviate from the frequency-dependent phonon MC simulations. However, the difference is still within 14% for $p/w \leq 10$.

Along another line, the thermal resistance of the rectangular-nanowire neck region is neglected in the derivation of Eq. (14a). With large b values, this assumption becomes less accurate. In this situation, the overall thermal resistance R_L of a single period is

$$R_L = R_{\text{slot}} + R_b, \quad (26)$$

where R_{slot} represents the thermal resistance of a single period with $b \to 0$. In the calculation of $R_{\text{slot}} = l/ptk_L$

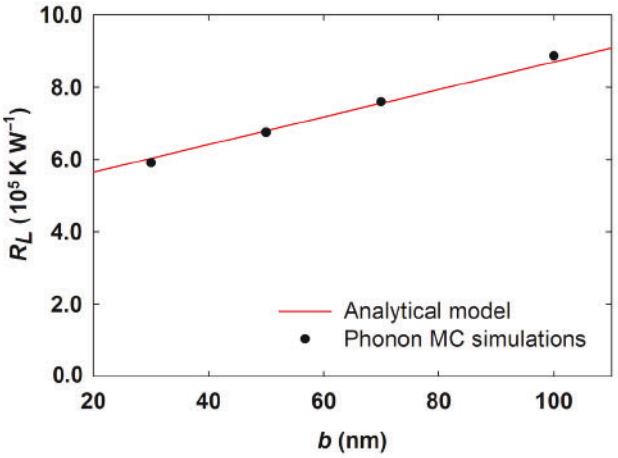

FIG. 6. Comparison between the analytical model and frequency-dependent phonon MC simulations on the thermal resistance R_L of a single period with increased b values. Other dimensions are $p = 400$ nm, $w = 100$ nm, $t = 100$ nm, and $l - b = 190$ nm.

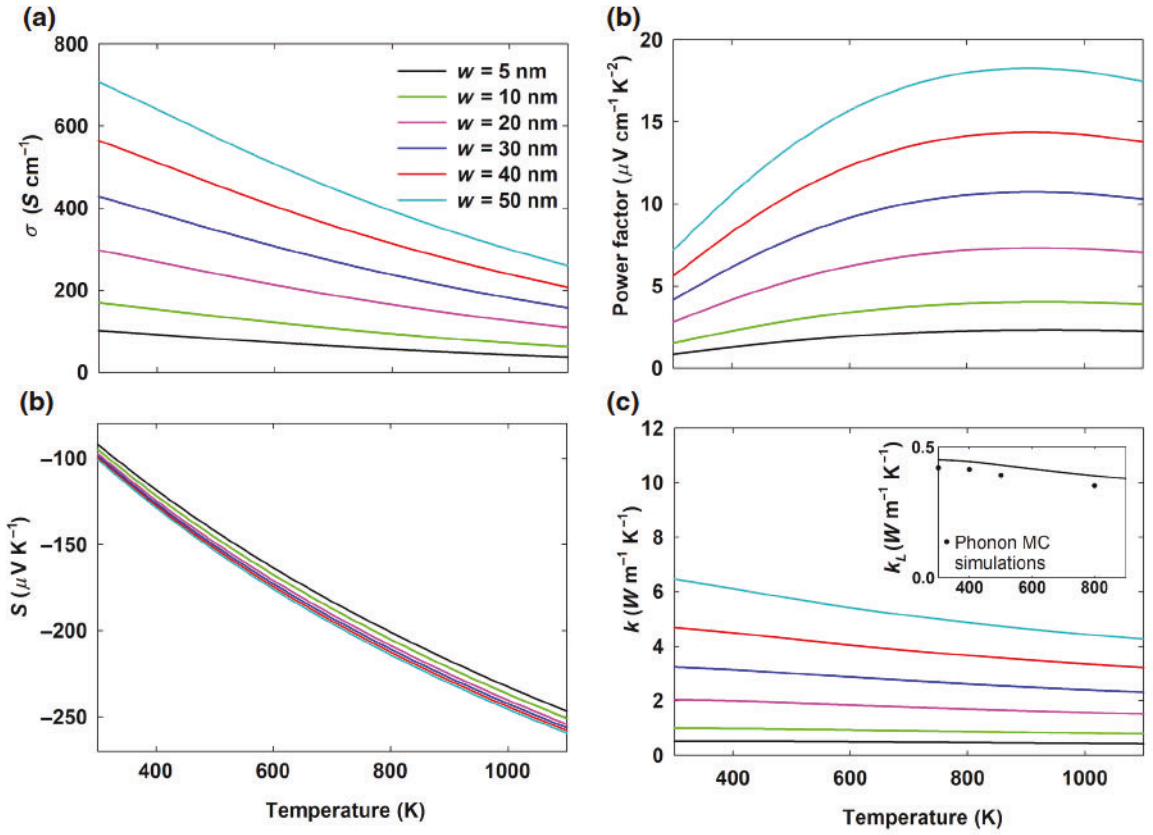

FIG. 7. Temperature-dependent TE properties for periodic nanoslot-patterned Si thin films: (a) in-plane electrical conductivity σ, (b) Seebeck coefficient S, (c) power factor, (d) in-plane lattice thermal conductivity k (inset, the lattice thermal conductivity k_L for the $w = 5$ nm case compared to that predicted by frequency-dependent phonon MC simulations). Dimensions include $p = 100$ nm, $l = 20$ nm, $t = 50$ nm, $b = 2$ nm, and $w = 5$–50 nm.

based on Eq. (16) and Eq. (14a), the required H_w can be obtained at an ultrasmall b value. The additional thermal resistance associated with the depth b of the neck region is denoted as R_b, which can be treated as the thermal resistance of a rectangular nanowire with w, t, and b as its width, thickness, and length, respectively. To solve for R_b, a two-step model [45] is employed, which is well calibrated with frequency-dependent phonon MC simulations. In this model, Eq. (15) is first used to modify Λ_{bulk} with t as the film thickness, leading to Λ_{film}. Then Eq. (15) is used again to modify Λ_{film} with w as the second film thickness to obtain the phonon MFP Λ_{wire} within the rectangular nanowire. The kinetic relationship can thus be used to calculate the lattice thermal conductivity k_{wire} for the nanowire, yielding $R_b = b/wtk_{\text{wire}}$. With R_{slot} and R_b, R_L can be acquired to compute the corresponding lattice thermal conductivity. Figure 6 presents a comparison between R_L determined using Eq. (26) and R_L obtained from frequency-dependent phonon MC simulations. The dimensions used in Fig. 6 are $p = 400$ nm, $w = 100$ nm, and $t = 100$ nm. The distance $(l - b)$ is fixed at 190 nm, while b increases from 30 to 100 nm in phonon MC simulations. Good agreement is found between the analytical model and the phonon MC simulations, validating Eq. (26) in determining R_L and thus k_L for nanoslot patterns with a large b. Based on the average temperature drop and counted phonon energy flow through the neck region, R_b extracted from frequency-dependent phonon MC simulations diverges within 4% from R_b computed with the two-step model.

C. TE properties predicted for nanoslot-patterned Si thin films

The proposed model is utilized to predict the TE properties of a nanoslot-patterned n-type Si thin film (Fig. 1). The calculated structures have dimensions of $l = 20$ nm, $p = 100$ nm, $b = 2$ nm, $t = 50$ nm, and $w = 5$–50 nm. A doping level of 2×10^{20} cm^{-3} is considered for n-type Si, with sixfold degenerate nonparabolic conduction bands and a parabolic spherical valence band. Due to the lack of temperature dependence of first-principles phonon MFPs [52], fitted bulk phonon MFPs given by Wang *et al.* [57] is adopted and further modified for heavily doped Si. Three identical isotropic and sine-shaped acoustic phonon branches are assumed. The considered phonon-scattering

mechanisms include the Umklapp scattering, the impurity scattering and the charge-carrier scattering. The Umklapp scattering rates are given by Wang *et al.* [57]. For the impurity-phonon scattering rate, given as $1/\tau_{\rm im} = A\omega^4$ [58,59], the constant $A = 1.647 \times 10^{-44}\,{\rm s}^3$ is estimated based on the studies by Asheghi *et al.* for heavily doped single-crystal Si films [60]. The charge-carrier scattering expression is given by Ziman [59]. Detailed information regarding the adopted scattering rates and phonon MFPs can be found elsewhere [43,49,58].

Temperature-dependent TE properties from room temperature to 1100 K are presented in Fig. 7. Various w values are represented by curves with different colors. Other dimensions include $p = 100$ nm, $l = 20$ nm, $t = 50$ nm, and $b = 2$ nm. In Fig. 7(a), the σ reduction is mainly due to the small correction factor H_w that is around 0.11 for $w = 5$ nm. Figure 7(b) shows the temperature-dependent Seebeck coefficients S. Because S heavily depends on the doping level instead of the modified electron MFPs [61], slight difference can be found between curves with varied w values. The power factor peaks at around 900 K for these samples, as displayed in Fig. 7(c). For k shown in Fig 7(c), a remarkable reduction can be found with decreased w values. In addition, the k_L predictions are also validated by frequency-dependent phonon MC simulations for $w = 5$ nm. In Fig. 7(d) inset, reasonably good agreement is found between the analytical model and the phonon MC simulations though some inaccuracy is anticipated for a large ratio $p/w = 20$.

The temperature-dependent ZTs are calculated and plotted in Fig. 8, in comparison with other experimental data. With $w = 5$ nm, a room temperature $ZT = 0.05$ and a maximum $ZT = 0.58$ at 1100 K are obtained. For the largest $w = 50$ nm, a $ZT = 0.45$ at 1100 K can still be achieved. In comparison, experimental results for nanostructured bulk Si are also plotted in Fig. 8. Zhu *et al.* reported a $ZT = 0.46$ at 1060 K for n-type nanostructured bulk Si [62]. Yusufu *et al.* reported a lower $ZT = 0.35$ at 1050 K for n-type nanostructured bulk Si with an electron concentration of $3.84 \times 10^{20}\,{\rm cm}^{-3}$ at 300 K [63]. Petermann *et al.* reported a peak $ZT = 0.15$ at 700 K for samples made from plasma-synthesized Si nanoparticles with a nominal phosphorous dopant concentration of $5 \times 10^{20}\,{\rm cm}^{-3}$ [64]. Bux *et al.* studied the TE properties of a series of n-type nanostructured bulk Si samples [65]. For these samples, $ZT \approx 0.023$ at room temperature is measured and the highest ZT value surpassed that for a nanoslot-patterned thin film at elevated temperatures. At 600 K, the $w = 5$ nm pattern renders a ZT that is 40% higher than that reported by Zhu *et al.* [62].

Although nanoslot-patterned thin films may not provide a significant ZT improvement over some nanostructured bulk Si samples, these films have advantages in their materials design and exact structure-property control during the fabrication processes. These films can be fully integrated with Si devices for cooling applications, as suggested for thin films with periodic circular pores [66]. In addition, the in-plane thermal anisotropy within nanoslot-patterned films can also be employed to better guide the heat flow in certain applications [45]. One concern for the high-temperature applications of nanostructured materials is the thermal stability of the structure. In previous studies on electrochemically etched Si with irregular nanopores, the nanoporous structures can deform during the annealing process at 673 K for 45 min [67]. For nanoporous thin films, such a nanopore deformation can be minimized with a well-selected substrate that can prevent the spreading of softened Si at elevated temperatures. When a nanoporous Si thin film is placed on a thermally insulated SiO_2 substrate, the possible nanopore contraction can be largely suppressed even at 1173 K [68].

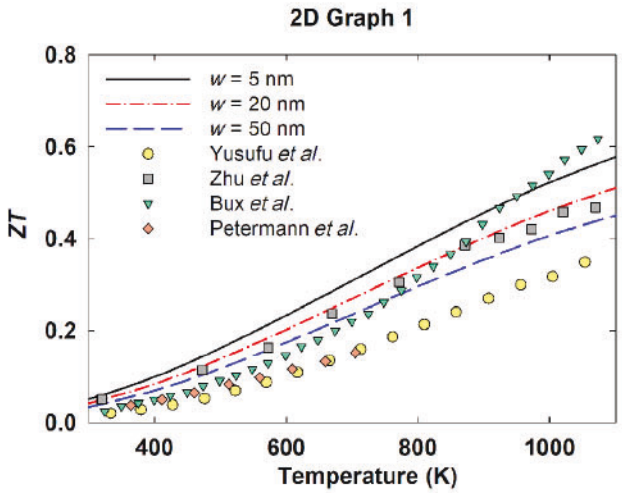

FIG. 8. Temperature-dependent ZTs of nanoslot patterns with varied neck widths, in comparison with experimental results from Yusufu *et al.* [63], Zhu *et al.* [62], Bux *et al.* [65], and Petermann *et al.* [64].

D. Approaches to further improve ZTs

Based on Eq. (14a), the neck width w can be largely reduced to decrease L_c and subsequently increase ZTs. When this L_c is still longer than majority electron MFPs, ZTs can always be enhanced with decreased L_c. A systemic study on L_c, k_L, and ZT with respect to the key geometric parameters is carried out here. Figure 9(a) shows the dependence of L_c on w and l, with fixed $p = 100$ nm. In Fig. 9(a), the minimum $L_c = 7.3$ nm is found at $w = 5$ nm and $l = 20$ nm. For $w = 1$ nm and $l = 10$ nm, a further reduced $L_c = 2.9$ nm can be obtained. Assuming $b = 2$ nm and $t = 50$ nm, the corresponding room-temperature k_L dependency on w and l is also presented in Fig. 9(b). As another factor to determine k_L, H_w monotonously increases with an increased L_c for the varied w and l values. At 300 K, the highest k_L is around $39\,{\rm W\,m^{-1}\,K^{-1}}$ as that for the initial solid film, i.e., $w = p$ and $L_c \to \infty$ in Eq. (14a).

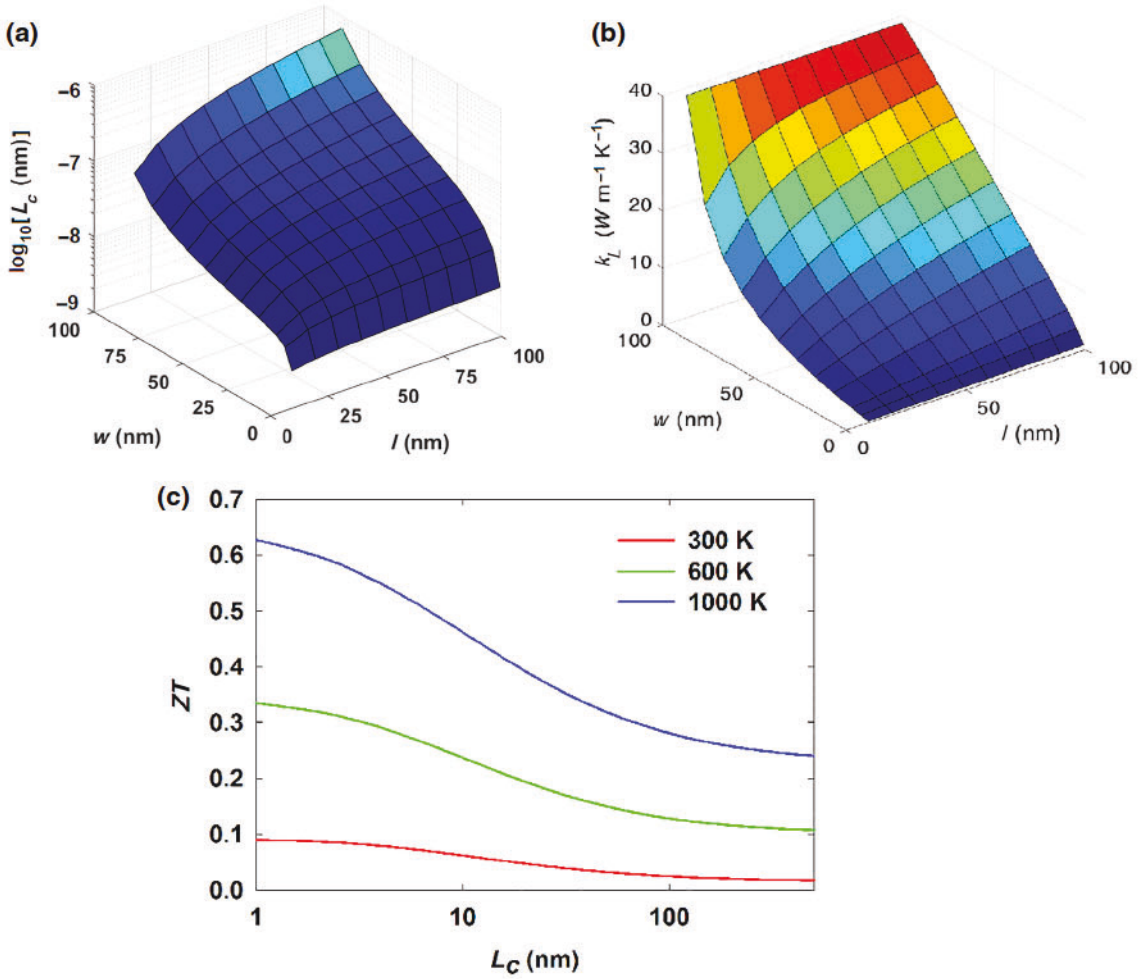

FIG. 9. (a) L_c dependence on w and l, with fixed $p = 100$ nm. (b) Room-temperature k_L dependence on w and l, with fixed $p = 100$ nm and $t = 50$ nm. (c) ZT as a function of L_c at three different temperatures, with $b = 2$ nm and $t = 50$ nm.

In addition, ZTs as a function of L_c is presented in Fig. 9(c). Here $ZT > 0.6$ can be achieved at 1000 K for $L_c = 1$ nm.

With the current L_c value, the calculated ZTs are close to the maximum $ZT \approx 0.64$ at 1000 K, as predicted for nano-sized Si at the small-nanostructure-size limit [36,48]. At this limit, the characteristic length L_c of a nanostructure is decreased to the MFPs of majority charge carriers so that ZT is maximized. Further reducing L_c does not affect the ZT when only semiclassical effects are considered. In this case, both k and σ will scale down with L_c, whereas S is determined by the doping level and remains as a constant.

In addition to nanoslot patterns, ZTs can be further enhanced through materials engineering. A higher doping level can also be used to enhance ZTs for materials like Si, resulting from a higher carrier concentration and a lower k_L due to enhanced impurity-phonon and electron-phonon scattering [69]. Along this line, a higher ZT is achieved using GaP to increase the bulk solubility limit of phosphorus from 1 at. % to 2.5 at. % [62]. Along another line, alloying Si with Ge atoms can also benefit ZTs due to a reduced k_L but the materials cost can be increased [62].

E. Extension to other geometries

Beyond the nanoslot-patterned thin films, the proposed analytical model can also be applied to other structures. Figure 10 presents the top view of a typical nanoslot-patterned thin film with a larger b value, i.e., a film with periodic rectangular nanopores. Phonon transport analysis of such films can be found in one study but a simple analytical expression of k_L is unavailable [34]. Two structures studied before can be produced by cutting a strip out of the porous thin film. In inset A, a fishbone nanowire [70] can be produced when the heat conduction channel lies in the middle of the strip. The fishbone nanowire consists of a nanowire and small wings that are perpendicular to the nanowire to distract the heat. In inset B, a nanoladder [56] can be formed when the rectangular nanopores lie in the middle of the strip. Both structures can be analyzed with

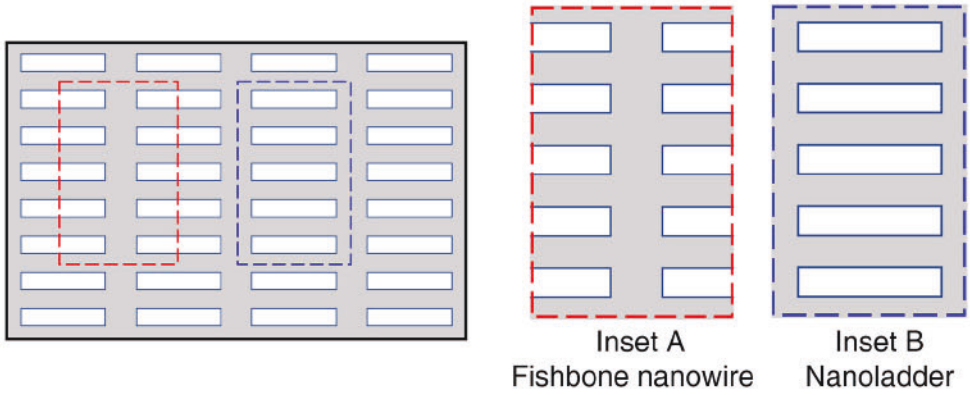

FIG. 10. Film with periodic rectangular nanopores and two representative thin-film-based structures cut out of this film (as two insets).

Eq. (26) with reasonably good accuracy. Slight overestimation of k_L is anticipated because the left and right sidewalls of these two structures should diffusively scatter phonon as real boundaries. In the periodic rectangular-nanopore film, these sidewalls as virtual boundaries are assumed to specularly scatter phonons due to the structural symmetry.

IV. CONCLUSIONS

In summary, an analytical model is proposed to accurately and quickly predict the TE properties of thin films or atomic layer materials with periodic nanoslot patterns. The analytical model modifies the phonon and charge-carrier MFPs with a characteristic length, as the classical size effects. Comparing with the technically demanding phonon MC simulations or other BTE solvers, the proposed model can be easily implemented to provide fast and high-throughput predictions, which is especially beneficial to the materials design. Frequency-dependent phonon MC simulations is used to verify the lattice thermal conductivity predictions by the analytical model. The analytical model is further examined for its accuracy for largely varied nanoslot patterns. In demonstration, TE properties of representative nanoslot patterns are calculated. A $ZT = 0.58$ at 1100 K is found for n-type Si thin films with a neck width $w = 5$ nm. Further structure optimization for ZT improvement is also performed using the analytical model.

This simple analytical model, which is based on L_c in Eq. (14a), is easy to be implemented for ZT evaluations. The results are practically interchangeable with the time-consuming and technically demanding phonon and electron MC simulations. The proposed model can easily predict TE properties of thin films with periodic rectangular pores, with extension to structures like fishbone nanowires and nanoladders.

ACKNOWLEDGMENTS

The authors thank Dr. Hongbo Zhao, Sien Wang, and Qiyu Chen for the technical assistance, and the University of Arizona Research computing High Performance Computing (HPC) and High Throughput Computing (HTC) for the allocation of computing time. This work is supported by the U.S. Air Force Office of Scientific Research (Grant No. FA9550-16-1-0025) for studies of nanoporous structures, and the National Science Foundation (Grant No. CBET-1651840) for studies on MC simulations.

[1] C. J. Vineis, A. Shakouri, A. Majumdar, and M. G. Kanatzidis, Nanostructured thermoelectrics: Big efficiency gains from small features, Adv. Mater. **22**, 3970 (2010).
[2] D. G. Cahill, P. V. Braun, G. Chen, D. R. Clarke, S. Fan, K. E. Goodson, P. Keblinski, W. P. King, G. D. Mahan, A. Majumdar, et al., Nanoscale thermal transport. II. 2003–2012, Appl. Phys. Rev. **1**, 011305 (2014).
[3] H. J. Goldsmid, *Thermoelectric Refrigeration* (Plenum, New York, 1964).
[4] A. J. Minnich, M. S. Dresselhaus, Z. F. Ren, and G. Chen, Bulk nanostructured thermoelectric materials: Current research and future prospects, Energy Environ. Sci. **2**, 466 (2009).
[5] G. J. Snyder and E. S. Toberer, Complex thermoelectric materials, Nat. Mater. **7**, 105 (2008).
[6] Z. Liu, J. Mao, T.-H. Liu, G. Chen, and Z. Ren, Nano-microstructural control of phonon engineering for thermoelectric energy harvesting, MRS Bull. **43**, 181 (2018).
[7] J.-H. Bahk, Z. Bian, and A. Shakouri, Electron energy filtering by a nonplanar potential to enhance the thermoelectric power factor in bulk materials, Phys. Rev. B **87**, 075204 (2013).
[8] B. Poudel, Q. Hao, Y. Ma, Y. Lan, A. Minnich, B. Yu, X. Yan, D. Wang, A. Muto, D. Vashaee, et al., High-thermoelectric performance of nanostructured bismuth antimony telluride bulk alloys, Science **320**, 634 (2008).
[9] K. Biswas, J. He, I. D. Blum, C.-I. Wu, T. P. Hogan, D. N. Seidman, V. P. Dravid, and M. G. Kanatzidis, High-performance bulk thermoelectrics with all-scale hierarchical architectures, Nature **489**, 414 (2012).
[10] J. Tang, H.-T. Wang, D. H. Lee, M. Fardy, Z. Huo, T. P. Russell, and P. Yang, Holey silicon as an efficient thermoelectric material, Nano Lett. **10**, 4279 (2010).
[11] J.-K. Yu, S. Mitrovic, D. Tham, J. Varghese, and J. R. Heath, Reduction of thermal conductivity in phononic nanomesh structures, Nat. Nanotechnol. **5**, 718 (2010).

[12] J. Lim, H.-T. Wang, J. Tang, S. C. Andrews, H. So, J. Lee, D. H. Lee, T. P. Russell, and P. Yang, Simultaneous thermoelectric property measurement and incoherent phonon transport in holey silicon, ACS Nano **10**, 124 (2016).
[13] L. Yang, N. Yang, and B. Li, Reduction of thermal conductivity by nanoscale 3D phononic crystal, Sci. Rep. **3**, 1143 (2013).
[14] L. Yang, N. Yang, and B. Li, Extreme Low thermal conductivity in nanoscale 3D Si phononic crystal with spherical pores, Nano Lett. **14**, 1734 (2014).
[15] M. R. Wagner, B. Graczykowski, J. S. Reparaz, A. El Sachat, M. Sledzinska, F. Alzina, and C. M. Sotomayor Torres, Two-Dimensional phononic crystals: Disorder matters, Nano Lett. **16**, 5661 (2016).
[16] J. Nakagawa, Y. Kage, T. Hori, J. Shiomi, and M. Nomura, Crystal structure dependent thermal conductivity in two-dimensional phononic crystal nanostructures, Appl. Phys. Lett. **107**, 023104 (2015).
[17] N. Zen, T. A. Puurtinen, T. J. Isotalo, S. Chaudhuri, and I. J. Maasilta, Engineering thermal conductance using a two-dimensional phononic crystal, Nat. Commun. **5**, 3435 (2014).
[18] P. E. Hopkins, C. M. Reinke, M. F. Su, R. H. Olsson, E. A. Shaner, Z. C. Leseman, J. R. Serrano, L. M. Phinney, and I. El-Kady, Reduction in the thermal conductivity of single crystalline silicon by phononic crystal patterning, Nano Lett. **11**, 107 (2010).
[19] D. Xu, S. Tang, X. Du, and Q. Hao, Detecting the major charge-carrier scattering mechanism in graphene antidot lattices, Carbon **144**, 601 (2019).
[20] Y. Yan, Q.-F. Liang, H. Zhao, C.-Q. Wu, and B. Li, Thermoelectric properties of one-dimensional graphene antidot arrays, Phys. Lett. A **376**, 2425 (2012).
[21] J. Oh, H. Yoo, J. Choi, J. Y. Kim, D. S. Lee, M. J. Kim, J.-C. Lee, W. N. Kim, J. C. Grossman, and J. H. Park, Significantly reduced thermal conductivity and enhanced thermoelectric properties of single- and bi-layer graphene nanomeshes with sub-10 nm neck-width, Nano Energy **35**, 26 (2017).
[22] Q. Hao, Y. Xiao, and H. Zhao, Characteristic length of phonon transport within periodic nanoporous thin films and two-dimensional materials, J. Appl. Phys. **120**, 065101 (2016).
[23] D. Xu, Q. Wang, X. Wu, J. Zhu, H. Zhao, B. Xiao, X. Wang, X. Wang, and Q. Hao, Largely reduced cross-plane thermal conductivity of nanoporous $In_{0.1}Ga_{0.9}N$ thin films directly grown by metalorganic chemical vapor deposition, Front. Energy **12**, 127 (2018).
[24] Y.-C. Hua and B.-Y. Cao, Anisotropic heat conduction in Two-dimensional periodic silicon nanoporous films, J. Phys. Chem. C **121**, 5293 (2017).
[25] K. D. Parrish, J. R. Abel, A. Jain, J. A. Malen, and A. J. McGaughey, Phonon-boundary scattering in nanoporous silicon films: Comparison of monte carlo techniques, J. Appl. Phys. **122**, 125101 (2017).
[26] S. Alaie, D. F. Goettler, M. Su, Z. C. Leseman, C. M. Reinke, and I. El-Kady, Thermal transport in phononic crystals and the observation of coherent phonon scattering at room temperature, Nat. Commun. **6**, 7228 (2015).
[27] P. E. Hopkins, L. M. Phinney, P. T. Rakich, R. H. Olsson, and I. El-Kady, Phonon considerations in the reduction of thermal conductivity in phononic crystals, Appl. Phys. A **103**, 575 (2011).
[28] P. E. Hopkins, P. T. Rakich, R. H. Olsson, I. F. El-Kady, and L. M. Phinney, Origin of reduction in phonon thermal conductivity of microporous solids, Appl. Phys. Lett. **95**, 161902 (2009).
[29] C. Huang, X. Zhao, K. Regner, and R. Yang, Thermal conductivity model for nanoporous thin films, Phys. E Low-Dimens. Syst. Nanostruct. **97**, 277 (2018).
[30] Q. Hao, Y. Xiao, and Q. Chen, Determining phonon mean free path spectrum by ballistic phonon resistance within a nanoslot-patterned thin film, Mater. Today Phys. **10**, 100126 (2019).
[31] B.-Y. Cao, W.-J. Yao, and Z.-Q. Ye, Networked nanoconstrictions: An effective route to tuning the thermal transport properties of graphene, Carbon **96**, 711 (2016).
[32] F. Domínguez-Adame, M. Martín-González, D. Sánchez, and A. Cantarero, Nanowires: A route to efficient thermoelectric devices, Phys. E Low-Dimens. Syst. Nanostruct. **113**, 213 (2019).
[33] Q. Hao, G. Chen, and M.-S. Jeng, Frequency-dependent monte carlo simulations of phonon transport in two-dimensional porous silicon with aligned pores, J. Appl. Phys. **106**, 114321/1 (2009).
[34] J. Lee, W. Lee, G. Wehmeyer, S. Dhuey, D. L. Olynick, S. Cabrini, C. Dames, J. J. Urban, and P. Yang, Investigation of phonon coherence and backscattering using silicon nanomeshes, Nat. Commun. **8**, 14054 (2017).
[35] C. Bi and B. Fu, Thermal conduction in nano-porous silicon thin film, J. Appl. Phys. **114**, 184302 (2013).
[36] C. Bera, M. Soulier, C. Navone, G. Roux, J. Simon, S. Volz, and N. Mingo, Thermoelectric properties of nanostructured $Si_{1-x}Ge_x$ and potential for further improvement, J. Appl. Phys. **108**, 124306 (2010).
[37] A. Jain, Y.-J. Yu, and A. J. H. McGaughey, Phonon transport in periodic silicon nanoporous films with feature sizes greater than 100 nm, Phys. Rev. B **87**, 195301 (2013).
[38] Y. Xiao, Q. Chen, D. Ma, N. Yang, and Q. Hao, Phonon transport within periodic porous structures–from classical phonon size effects to wave effects, ES Mater. Manuf. **5**, 2 (2019).
[39] A. Eucken, Thermal conductivity of ceramic refractory materials: Calculation from thermal conductivity of constituents, Ceram. Abstr. **11**, 576 (1932).
[40] A. Eucken, Thermal conductivity of ceramic refractory materials: Calculation from thermal conductivity of constituents, Ceram. Abstr. **12**, 231 (1933).
[41] Z. Hashin and S. Shtrikman, A variational approach to the theory of the effective magnetic permeability of multiphase materials, J. Appl. Phys. **33**, 3125 (1962).
[42] G. Chen, *Nanoscale Energy Transport and Conversion: A Parallel Treatment of Electrons, Molecules, Phonons, and Photons* (Oxford University Press, New York, 2005).
[43] J. M. Ziman, *Electrons and phonons: the theory of transport phenomena in solids* (Oxford University Press, Oxford, England, 2001).
[44] Z. M. Zhang, *Nano/microscale heat transfer* (McGraw-Hill, New York, 2007).

[45] Q. Hao, Y. Xiao, and S. Wang, Two-step modification of phonon mean free paths for thermal conductivity predictions of thin-film-based nanostructures, Int. J. Heat Mass Transfer **153**, 119636 (2020).
[46] E. O. Kane, Band structure of indium antimonide, J. Phys. Chem. Solids **1**, 249 (1957).
[47] J. Kolodziejczak, Transport of current carriers in n-type indium antimonide at low temperatures, Acta Phys. pol. **20**, 289 (1961).
[48] Q. Hao, D. Xu, N. Lu, and H. Zhao, High-throughput ZT predictions of nanoporous bulk materials as next-generation thermoelectric materials: A material genome approach, Phys. Rev. B **93**, 205206 (2016).
[49] Q. Hao, H. Zhao, and D. Xu, Thermoelectric studies of nanoporous thin films with adjusted pore-edge charges, J. Appl. Phys. **121**, 094308 (2017).
[50] Q. Hao and Y. Xiao, Electron monte carlo simulations of nanoporous Si thin films—The influence of pore-edge charges, J. Appl. Phys. **125**, 064301 (2019).
[51] J.-P. M. Péraud and N. G. Hadjiconstantinou, Efficient simulation of multidimensional phonon transport using energy-based variance-reduced monte carlo formulations, Phys. Rev. B **84**, 205331 (2011).
[52] K. Esfarjani, G. Chen, and H. T. Stokes, Heat transport in silicon from first-principles calculations, Phys. Rev. B **84**, 085204 (2011).
[53] Y. Hu, L. Zeng, A. J. Minnich, M. S. Dresselhaus, and G. Chen, Spectral mapping of thermal conductivity through nanoscale ballistic transport, Nat. Nanotechnol. **10**, 701 (2015).
[54] F. Yang and C. Dames, Mean free path spectra as a tool to understand thermal conductivity in bulk and nanostructures, Phys. Rev. B **87**, 035437 (2013).
[55] G. Romano and J. C. Grossman, Heat conduction in nanostructured materials predicted by phonon bulk mean free path distribution, J. Heat Transfer **137**, 071302 (2015).
[56] W. Park, J. Sohn, G. Romano, T. Kodama, A. Sood, J. S. Katz, B. S. Y. Kim, H. So, E. C. Ahn, M. Asheghi, et al., Impact of thermally dead volume on phonon conduction along silicon nanoladders, Nanoscale **10**, 11117 (2018).
[57] Z. Wang, J. E. Alaniz, W. Jang, J. E. Garay, and C. Dames, Thermal conductivity of nanocrystalline silicon: Importance of grain size and frequency-dependent mean free paths, Nano Lett. **11**, 2206 (2011).
[58] P. G. Klemens, The scattering of Low-frequency lattice waves by static imperfections, Proc. Phys. Soc. A **68**, 1113 (1955).
[59] J. M. Ziman, Xvii. The effect of free electrons on lattice conduction, Philos. Mag. A **1**, 191 (1956).
[60] M. Asheghi, K. Kurabayashi, R. Kasnavi, and K. E. Goodson, Thermal conduction in doped single-crystal silicon films, J. Appl. Phys. **91**, 5079 (2002).
[61] G. Chen, *Nanoscale Energy Transport and Conversion : A Parallel Treatment of Electrons, Molecules, Phonons, and Photons* (Oxford University Press Inc, New York, United States, 2005).
[62] G. H. Zhu, H. Lee, Y. C. Lan, X. W. Wang, G. Joshi, D. Z. Wang, J. Yang, D. Vashaee, H. Guilbert, A. Pillitteri, et al., Increased phonon scattering by nanograins and point defects in nanostructured silicon with a Low concentration of germanium, Phys. Rev. Lett. **102**, 196803 (2009).
[63] A. Yusufu, K. Kurosaki, Y. Miyazaki, M. Ishimaru, A. Kosuga, Y. Ohishi, H. Muta, and S. Yamanaka, Bottom-up nanostructured bulk silicon: A practical high-efficiency thermoelectric material, Nanoscale **6**, 13921 (2014).
[64] N. Petermann, N. Stein, G. Schierning, R. Theissmann, B. Stoib, M. S. Brandt, C. Hecht, C. Schulz, and H. Wiggers, Plasma synthesis of nanostructures for improved thermoelectric properties, J. Phys. D: Appl. Phys. **44**, 174034 (2011).
[65] S. K. Bux, R. G. Blair, P. K. Gogna, H. Lee, G. Chen, M. S. Dresselhaus, R. B. Kaner, and J.-P. Fleurial, Nanostructured bulk silicon as an effective thermoelectric material, Adv. Funct. Mater. **19**, 2445 (2009).
[66] Z. Ren and J. Lee, Thermal conductivity anisotropy in holey silicon nanostructures and its impact on thermoelectric cooling, Nanotechnology **29**, 045404 (2017).
[67] J. Salonen, E. Mäkilä, J. Riikonen, T. Heikkilä, and V. P. Lehto, Controlled enlargement of pores by annealing of porous silicon, Phys. Status Solidi (A) Appl. Mater. Sci. **206**, 1313 (2009).
[68] Q. Hao, Y. Xiao, and F. Medina, Annealing studies of nanoporous Si thin films fabricated by Dry Etch, ES Mater. Manuf. (2019).
[69] Q. Hao, G. Zhu, G. Joshi, X. Wang, A. Minnich, Z. Ren, and G. Chen, Theoretical studies on the thermoelectric figure of merit of nanograined bulk silicon, Appl. Phys. Lett. **97**, 063109 (2010).
[70] J. Maire, R. Anufriev, T. Hori, J. Shiomi, S. Volz, and M. Nomura, Thermal conductivity reduction in silicon fishbone nanowires, Sci. Rep. **8**, 4452 (2018).